Journal of Materials Chemistry A

ROYAL SOCIETY OF CHEMISTRY

PAPER

View Article Online
View Journal | View Issue

Cite this: J. Mater. Chem. A, 2025, 13, 17976

A Mo-cation/O-anion doping strategy for creating vacancy defects and cation multivalency to enhance the hydrogen evolution of ZnS under visible light†

Xinru Wu,‡[a] Tsz Lok Wan, ‡*[b] Baoqian Yang,[a] Dong-Hau Kuo, *[c] Pengkun Zhang,[a] Minghao Liu,[d] Samuel Ndaghiya Adawara,[a] Dongfang Lu,*[a] Jinguo Lin*[a] and Xiaoyun Chen *[a]

Herein, we designed a stable and photocorrosion-resistant Mo/O co-doped ZnS (labeled as ZnMoOS) catalyst with abundant sulfur vacancy (Vs) defects and bivalent Mo^{4+}/Mo^{6+} states for an effective photocatalytic hydrogen evolution reaction (photo-HER) under visible light. The Mo/O co-doping reduces the band gap of ZnS and extends its visible light absorption range. The hydrazine-driven process adjusts ZnMoOS with appropriate bivalent $n(Mo^{4+})/n(Mo^{6+})$ states and creates abundant Vs defects. The Vs defects are active sites to capture water molecules and weaken H–O–H bonds for producing protons and H_2 generation. The bivalent $n(Mo^{4+})/n(Mo^{6+})$ states act as hosts for photogenerated electrons, facilitating the rapid hopping of photogenerated electrons between $Mo^{4+} \leftrightarrow Mo^{6+}$ to transfer for the photo-HER, thereby improving the photo-HER efficiency. DFT calculations reveal that Mo/O co-doping of ZnMoOS with abundant Vs defects and heterovalent Mo^{4+}/Mo^{6+} states significantly facilitates hydrogen desorption and enhances the surface H* generation rate. ZnMoOS-3 with appropriate Mo/O co-doping and regulation with an optimum hydrazine content exhibits an excellent photo-HER rate of 41.6 mmol g^{-1} h^{-1} and an AQE of 18.6% at 400 nm, along with good durability and stability. This work provides a strategy for vacancy defects and heterovalent states for designing sulfide catalysts with high photo-HER activity and inhibition of photocorrosion.

Received 17th March 2025
Accepted 1st May 2025

DOI: 10.1039/d5ta02176f

rsc.li/materials-a

1. Introduction

Hydrogen has recently been considered an alternative to fossil energy sources due to its green nature and better energy capacity.[1–3] Coal and natural gas reforming are currently used in hydrogen gas generation. However, due to the challenges associated with environmental remediation and the lack of adequate production inspections in such processes, it has become a great source of concern because this production technique invariably involves using fossil fuels and environmental degradation.[4,5]

Photocatalytic hydrogen production has attracted significant attention due to its greater economic efficiency and environmental benefits compared to conventional hydrogen production strategies.[6,7] The photocatalytic water decomposition process comprises three primary steps. Firstly, upon light irradiation, electron–hole pairs are generated on the surface of the photocatalyst. Secondly, the charges undergo separation and migrate towards the photocatalyst surface. Finally, the electrons participate in redox reactions to generate hydrogen and reduce electron holes.[8,9] In 1972, Honda and Fujishima were the first to report hydrogen production by water decomposition on TiO_2 electrodes, and their research laid the theoretical groundwork for subsequent photocatalytic hydrogen production.[10] Subsequently, numerous semiconductor materials, such as TiO_2, NiO, ZnO, $SrTiO_3$, La:$NaTiO_3$, CdS and Ta_2O_5, were applied in the study of photocatalytic decomposition of water to produce hydrogen.[11–14] However, these are wide-bandgap semiconductors that can only be excited by ultraviolet radiation, which accounts for about 5% of the solar energy. Consequently, the effectiveness of solar-to-hydrogen conversion (STH) is

[a]College of Materials Engineering, Fujian Agriculture and Forestry University, Fuzhou 350002, China. E-mail: fjldf@126.com; fjlinjg@126.com; fjchenxy@126.com

[b]School of Mining and Petroleum Engineering, Department of Civil and Environmental Engineering, University of Alberta, Edmonton, AB, T6G 1H9, Canada. E-mail: twan1@ualberta.ca

[c]Department of Materials Science and Engineering, National Taiwan University of Science and Technology, Taipei 106335, Taiwan. E-mail: dhkuo@mail.ntust.edu.tw

[d]School of Mechanical, Medical and Process Engineering, Queensland University of Technology, Brisbane, QLD, AU 4000, Australia

† Electronic supplementary information (ESI) available. See DOI: https://doi.org/10.1039/d5ta02176f

‡ These authors contributed equally to this work.

relatively poor.[15] In contrast, narrow-bandgap photocatalysts can effectively utilize the photon energy of the visible light band for hydrogen production. Narrow band gap photocatalytic materials are highly promising for photocatalytic hydrogen production since the photon energy of the visible light band accounts for about 46% of the solar energy that reaches the Earth's surface. ZnS has been widely explored in the photo-HER, thanks to its rapid production rate of photo-induced e^- and h^+ pairs and a more negative U_{CB}-edge potential.[16] To improve the photocatalytic performance of ZnS, forming a Zn(O, S) solid solution by combining ZnS and ZnO has attracted considerable attention because of its abundant chemical resources, easy availability, environmental safety, and reusability.[17,18] Researchers such as Abdullah and Gultom have successfully enhanced the photocatalytic performance of the modified Zn(O, S) by doping it with Ho, Ni, Y, La, In, and Sn. The improved photocatalytic hydrogen evolution performance and the ability to reduce pollutants of Zn(O, S) indicate that Zn(O, S) materials have application prospects in the field of photocatalysis.[19–23] To further enhance the photocatalytic performance of Zn(O, S), researchers have adopted methods such as defect engineering.[24–26]

Defect engineering represents a promising approach for improving the light-trapping ability of photocatalytic materials like ZnS.[27–30] Vacancy defects have been demonstrated to broaden the absorption edge towards visible wavelengths while narrowing the overall band gap. During this process, visible light initially excites electrons from the VB to Vo energy level, which acts as the intermediate transition state. The electrons then shift to the conduction band, speeding up charge separation and transport and eventually enhancing the photocatalytic activity.[31–33] For instance, Wang *et al.*[34] demonstrated that an increase in vacancy defects results in a red shift of the absorption edge and an enhanced visible-light response. Moreover, there are numerous reports on improving the photocatalytic performance of ZnS through doping with transition metals and rare earth ions. Shah *et al.*[35] successfully prepared Sn-doped ZnS nanomaterials *via* the hydrothermal method, decreasing the bandgap from 3.50 eV to 3.10 eV. Lee *et al.*[36] successfully synthesized In/Cu co-doped ZnS nanoparticles in deionized water and ethanol solvent by a sonochemical method using citric acid as a surfactant in an aqueous medium, and the bandgap decreased from 3.74 eV to 3.59 eV. Bao *et al.*[37] prepared a series of Co-doped ZnS catalysts, and Co-doping reduced the bandgap of ZnS from 3.31 eV to 3.20 eV. Furthermore, doping ZnS with a second metal can further improve the efficiency of photocatalysts, as it helps to slow down the recombination of photogenerated electron–hole pairs.[38] Noble metals like Pt, Ir, Ru, Au, *etc.* have been reported to be the most efficient co-catalysts when doped onto semiconductors. However, their high cost and limited availability obstruct commercializing current photocatalysts for hydrogen production.[39] Hence, the research on developing active photocatalysts that are both cost-effective and relatively abundant has become a focal point in scientific research.

Molybdenum is relatively abundant, of low cost, and non-toxic.[40] Mo-doping can accelerate the electron transfer from the VB to CB, diminish the recombination of e^- and h^+, gain active sites on the photocatalyst surface, and significantly enhance the activity of the photocatalyst, thereby increasing the hydrogen generation rate.[41–43] Meanwhile, Mo-doping can also improve the stability of the photocatalyst, enabling it to maintain high activity even after repeated recycling.[44,45] For example, Zuo *et al.*[45] designed a Mo-doped $ZnIn_2S_4$ (MoZIS)-coated Ni-based Hofmann-type coordination polymer (Ni–NiHCP), and the H_2 yield of Ni–NiHCP/MoZIS reached 26.7 mmol g^{-1} h^{-1} under visible light irradiation, which was 10 times higher than that of pure ZIS. Tamboli *et al.*[46] fabricated a multi-component Mo-doped $BiVO_4$@graphite photoanode through a simple spin-coating and annealing process. By leveraging the synergistic effect between Mo and graphene, they improved the carrier density and inhibited photo-induced e^- and h^+ recombination rates to enhance the photo-HER efficiency. Li *et al.*[47] prepared Mo/S co-doped g-C_3N_4, which extended the photoresponse range and achieved an H_2 yield of 294 μmol g^{-1} h^{-1} without a noble metal co-catalyst. Nevertheless, the abovementioned reports have limitations, such as a relatively low H_2 yield, complex catalyst synthesis methods, or stringent photo-HER conditions.

Based on the above limitations, ZnMoOS was synthesized using hydrolysis at atmospheric pressure. ZnS was doped with Mo/O, and hydrazine was used as a reducing agent to reduce Mo^{6+} to Mo^{4+}, which broke the charge balance of the system to produce Vs. The synergistic effect of transition metal doping and sulfur defect engineering enhanced the photocatalytic performance of ZnMoOS.

2. Experimental

2.1 Preparation of catalysts

To a beaker containing 800 mL of distilled water, 20 mmol of $Na_2MoO_4 \cdot 2H_2O$ (A.R.), 10 mmol of $ZnCl_2$ (A.R.) and 10 mmol of thioacetamide (TAA, A.R.) were added sequentially, adding each component at an interval of 20 min. After increasing the temperature of the mixture to 98 °C, 0, 0.2, 0.4, and 0.6 mL of N_2H_4 (A.R. 85%) were individually added to the mixed solution to react at 98 °C for 3 h. The formed precipitates were washed with deionized H_2O and anhydrous C_2H_5OH five and three times, respectively, and dried at a rotary evaporator at 70 °C for 1 h. Then, the obtained solids were labeled as ZnMoOS-1, ZnMoOS-2, ZnMoOS-3, and ZnMoOS-4, respectively. For comparison, samples without $Na_2MoO_4 \cdot 2H_2O$ and with 0.4 mL of N_2H_4 (A.R. 85%) but without $Na_2MoO_4 \cdot 2H_2O$ were also prepared using the same synthetic process. These samples were labeled as ZnS and ZnOS, respectively.

2.2 Characterization of catalysts

The XPS test was performed on a PHI5700 ESCA system with Al Kα X-rays. UPS measurements were conducted with He I (21.22 eV) monochromatic light. The XRD test was carried out on a Rigaku Ultima IV phase-emission X-ray diffractometer (λ = 1.5405 Å). The EPR signal of DMPO was collected using a Bruker A300 spectrometer. A ZSX Primus II X-ray fluorescence

spectrometer was applied for elemental analysis. Ultraviolet-visible spectroscopy was carried out using a Lambda 750S spectrometer to measure the visible absorption spectrum of ultraviolet light. The FE-SEM test was performed on a Hitachi SU-8010 scanning electron microscope, and a TEM test was accomplished on a TECNAI G2 F20 transmission electron microscope. Optical property analysis was conducted on a Lambda 750S spectrophotometer with $BaSO_4$ (A.R.) as the reference. The specific surface area (S_{BET}) analysis was performed on an ASAP 2020 analyzer, and the S_{BET} was calculated using the BET formula. The pore-size distribution was determined using the BJH formula. Photoluminescence (PL) was carried out on a fluorescence spectrometer (Varian Cary Eclipse 500) with an excitation wavelength of 460 nm. The sulfur vacancies were investigated by Raman spectroscopy (HORIBA LabRAM HR 800), and electrochemical analyses were conducted on a BioLogic SP-300 utilizing the method reported in the literature.[1] The detailed measurement procedure is provided in the ESI.†

2.3 Evaluation of photocatalytic hydrogen activity

The photo-HER activity was assessed on a Labsolar-6A system (Perfect Light Co.) with a 300 W Xe lamp filtered at 420 nm. During the experiment, 50 mg of the catalyst was dispersed in a 50 mL aqueous solution containing 10 mmol of Na_2S and Na_2SO_3 as sacrificial agents. A dilute nitric acid solution was added dropwise and mixed evenly, and the pH was adjusted to 6.5. The reactor was degassed by argon purging and had a H_2O circulation cooling system to maintain the temperature of the reactor at 25 °C. The H_2 formation was analyzed using an online Panna A91 gas analyzer with 99.999% helium as the carrier gas under visible light irradiation for 6 h. The detailed AQE calculations are provided in the ESI.†

2.4 Density functional theory calculation method

The DFT calculation procedure is provided in detail in the ESI.†

3. Results and discussion

3.1 Structure analysis

Fig. 1a presents XRD patterns of ZnMoOS, ZnOS, and ZnS catalysts. We observe that diffraction peaks at 28.909°, 48.110°, 57.105°, and 77.830° correspond to crystal planes (111), (220), (311), and (331), respectively, of monoclinic ZnS phases indexed in PDF#80-0020. Notably, the diffraction patterns of ZnOS and ZnMoOS catalysts do not match the crystal planes of monoclinic zinc oxide, indicating their single-phase structure. The crystal sizes of ZnMoOS, ZnOS, and ZnS are calculated from the peak broadening in XRD patterns, and the results are included in Table S1.† It was revealed that Mo/O co-doping decreased the crystallinity of ZnS. Still, with increased hydrazine content, the grain size of ZnMoOS increases, and the contact area increases due to the reduction of Mo^{6+} to Mo^{4+} by hydrazine.

XPS has been employed to analyze the valence states and composition of elements on the ZnMoOS-3 surface. Fig. S1† displays the survey XPS spectrum of ZnMoOS-3, with peaks corresponding to Zn, Mo, S, and O elements. Fig. 1b shows that the peaks at 1022.3 and 1045.4 eV are related to Zn $2p_{3/2}$ and Zn $2p_{1/2}$, respectively.[48,49] Fig. 1c presents the S 2p spectra of ZnMoOS-3 and ZnOS. For ZnMoOS-3, the binding energy peaks are located at 161.8 eV and 163.8 eV, which are attributed to S $2p_{3/2}$ and S $2p_{1/2}$, respectively. Compared with ZnOS, these two peaks of ZnMoOS-3 shift towards the direction of lower binding energy, a phenomenon likely to be caused by the presence of Vs. The Vs facilitate electron transfer, thus reducing the binding energy.[50–54] Fig. 1d shows the photoelectron spectra of O 1s, indicating that oxygen is located in multiple chemical environments, with distinct binding energies observed for lattice oxygen ($O_{Lattice}$) and hydroxyl oxygen (O–H) at 529.9 and 531.4 eV, respectively.[55,56] By comparing the XPS spectra of Zn, O, and S in ZnMoOS-3 and ZnOS, it can be found that their binding energies all exhibit a negative shift. This indicates that Mo doping has altered the chemical environments of Zn, O, and S.[57] Fig. 1e shows that Mo exists in heterovalent states, with binding energies at 234.7 and 231.58 eV related to Mo^{4+} $3d_{3/2}$ and Mo^{4+} $3d_{5/2}$, respectively, while binding energies at 235.6 and 232.4 eV correspond to Mo^{6+} $3d_{3/2}$ and Mo^{6+} $3d_{5/2}$, respectively. Mo in ZnMoOS exhibits two valence states: Mo^{6+} and Mo^{4+}. The formation of Mo^{4+} leads to the creation of Vs and an increased charge transfer rate.[58,59] These results indicate an increase in Vs. Combined with the EPR data in Fig. 1f, the peak at $g = 2.004$ further confirms the formation of Vs in ZnMoOS.[60,61] The results further demonstrate that the formation of Vs can be enhanced by doping Mo and adjusting the valence states of Mo. The addition of hydrazine reduces Mo^{6+} to Mo^{4+} and leads to the reconstruction of valence charges. Therefore, Mo generates heterovalent states, forming a large amount of Vs to maintain the overall charge balance of the crystal. Notably, there is a significant synergistic effect between heterovalent states and Vs, which enhances the charge separation of photo-induced carriers, delays recombination, and prolongs their lifetime. Meanwhile, more active sites are formed on the catalyst surface, facilitating the adsorption, activation, and conversion of reactant molecules. This significantly boosts the photocatalytic performance, laying a solid foundation for its application in the photo-HER.

3.2 Morphology analysis

Fig. 2a and b depict the morphology of the ZnMoOS-3 catalyst at 50k and 30k magnifications, respectively, revealing a uniform accumulation of nanoparticles into powder clusters. Fig. 2c and d present SEM images of ZnOS, which exhibit a similar morphology to ZnMoOS-3, although the nanoparticle diameter of ZnOS is smaller. The TEM image of ZnMoOS-3 in Fig. 2e further confirms that ZnMoOS-3 comprises nanoparticles with an average size of 50 nm. Fig. 2f presents the HR-TEM image of ZnMoOS-3, with a *d*-spacing value of 3.09 Å related to the (111) crystal plane of ZnS (PDF# 80-0020). Fig. 2g shows a selected region for the SEM-EDS elemental mapping, and Fig. 2g–k display SEM-EDS elemental mapping images of ZnMoOS-3, indicating the uniform distribution of O and Mo elements in ZnMoOS-3. Meanwhile, Tables S1–S3† present Zn, Mo, O, and S

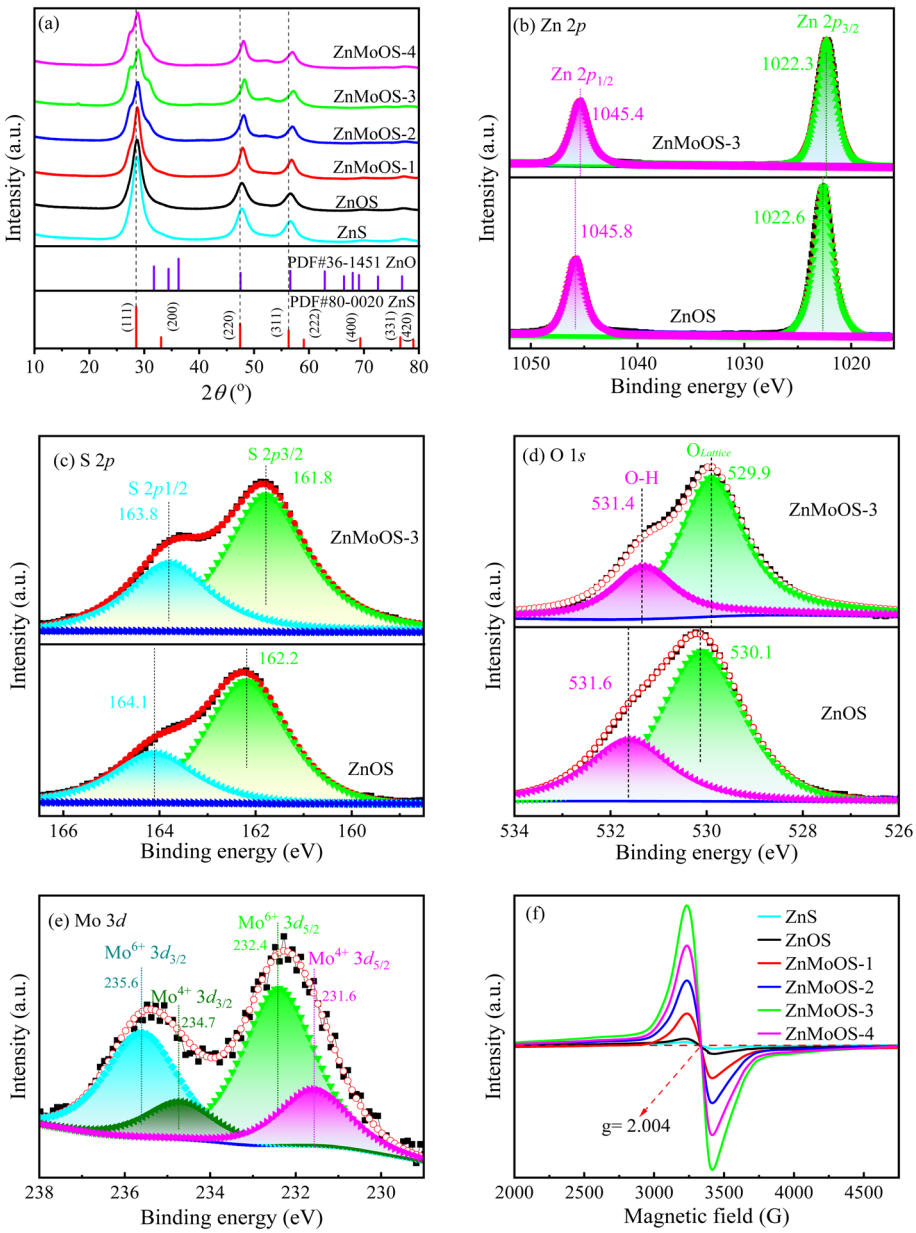

Fig. 1 (a) XRD spectra of ZnMoOS, ZnOS, and ZnS. The XPS spectra of (b) Zn 2p, (c) S 2p, (d) O 1s, and (e) Mo 3d. (f) EPR spectra of ZnMoOS, ZnOS, and ZnS.

elemental contents in the catalyst, as measured by XPS, XRF, and SEM-EDS, respectively. All the above-mentioned results were consistent.

BET and pore size distribution test results are presented in Fig. 2l. The BET curves display a hysteresis regression IV isotherm at a relative pressure (p/p^o) between 0.8 and 1.0.[62] The BJH pore size distribution curves are shown in Fig. 2m. The S_{BET} of ZnMoOS-3 was determined to be 64.7 $m^2\ g^{-1}$, the total pore volume was 0.032 $cm^3\ g^{-1}$, and the average pore diameter was 0.26 nm. In contrast, the S_{BET}, total pore volume, and average pore diameter of ZnOS were 35.9 $m^2\ g^{-1}$, 0.014 $cm^3\ g^{-1}$, and 0.13 nm, respectively. These results confirm that ZnMoOS-3 has higher S_{BET} than ZnOS, indicating more active sites and potentially superior photo-HER activity.

3.3 Energy band structure analysis

UV-vis spectra of ZnS, ZnOS, and ZnMoOS are shown in Fig. 3a. It is observed that ZnMoOS has a substantial absorption range in the visible region, while ZnS and ZnOS only absorb ultraviolet light. However, UV light accounts for only 5% of sunlight, and ZnS and ZnOS cannot utilize sunlight efficiently. In this study, hydrazine was used as a dopant. The doping of Mo/O into ZnS significantly improved the optical properties of ZnS without changing its main phase. ZnMoOS-3 shows the best light absorption ability. The E_g was calculated using the formula: $(\alpha h\nu)^2 = k(h\nu - E_g)$, where k is the absorbance constant, ν is the optical frequency, and h is Planck's constant,.[63,64] As illustrated in Fig. S2,† the E_{g_1} values of ZnMoOS-1, ZnMoOS-2, ZnMoOS-3, ZnMoOS-4, ZnOS, and ZnS are 3.45, 3.38, 3.36, 3.37, 3.50, and

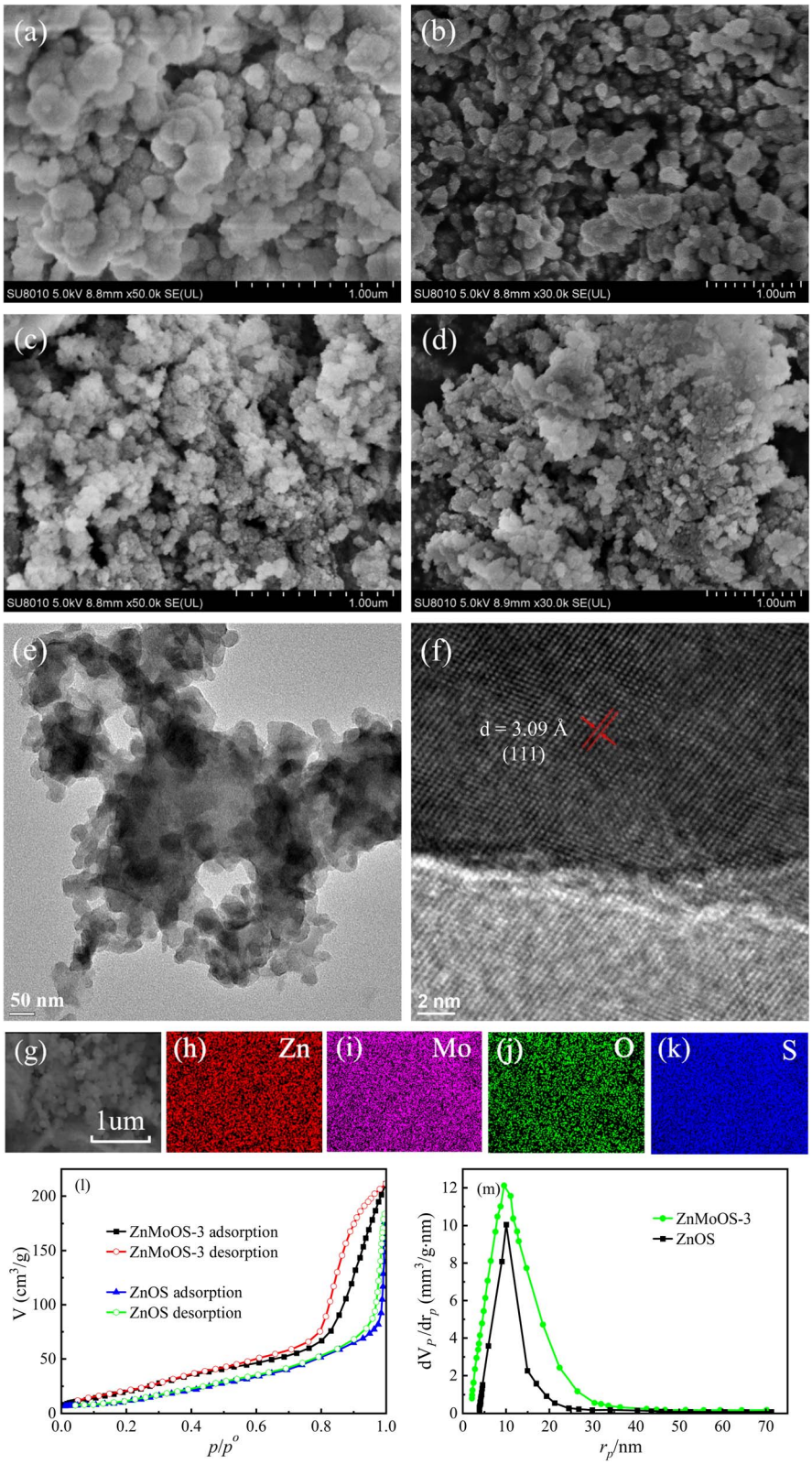

Fig. 2 SEM images of (a and b) ZnMoOS-3 and (c and d) ZnOS. (e) TEM and (f) HR-TEM images of ZnMoOS-3. (g–k) SEM-EDS elemental mapping of ZnMoOS-3. (l) N_2 adsorption–desorption isotherms and (m) pore size distribution curves of ZnMoOS-3 and ZnOS.

3.55 eV, respectively. Notably, upon the incorporation of Mo into the ZnOS lattice, new energy levels emerge at λ_2 for ZnMoOS-1, ZnMoOS-2, ZnMoOS-3, and ZnMoOS-4, with corresponding E_{g_2} values of 3.00, 2.92, 2.83, and 2.88 eV, respectively. These values are significantly lower than the bandgap widths of ZnOS and ZnS. This reduction in bandgap

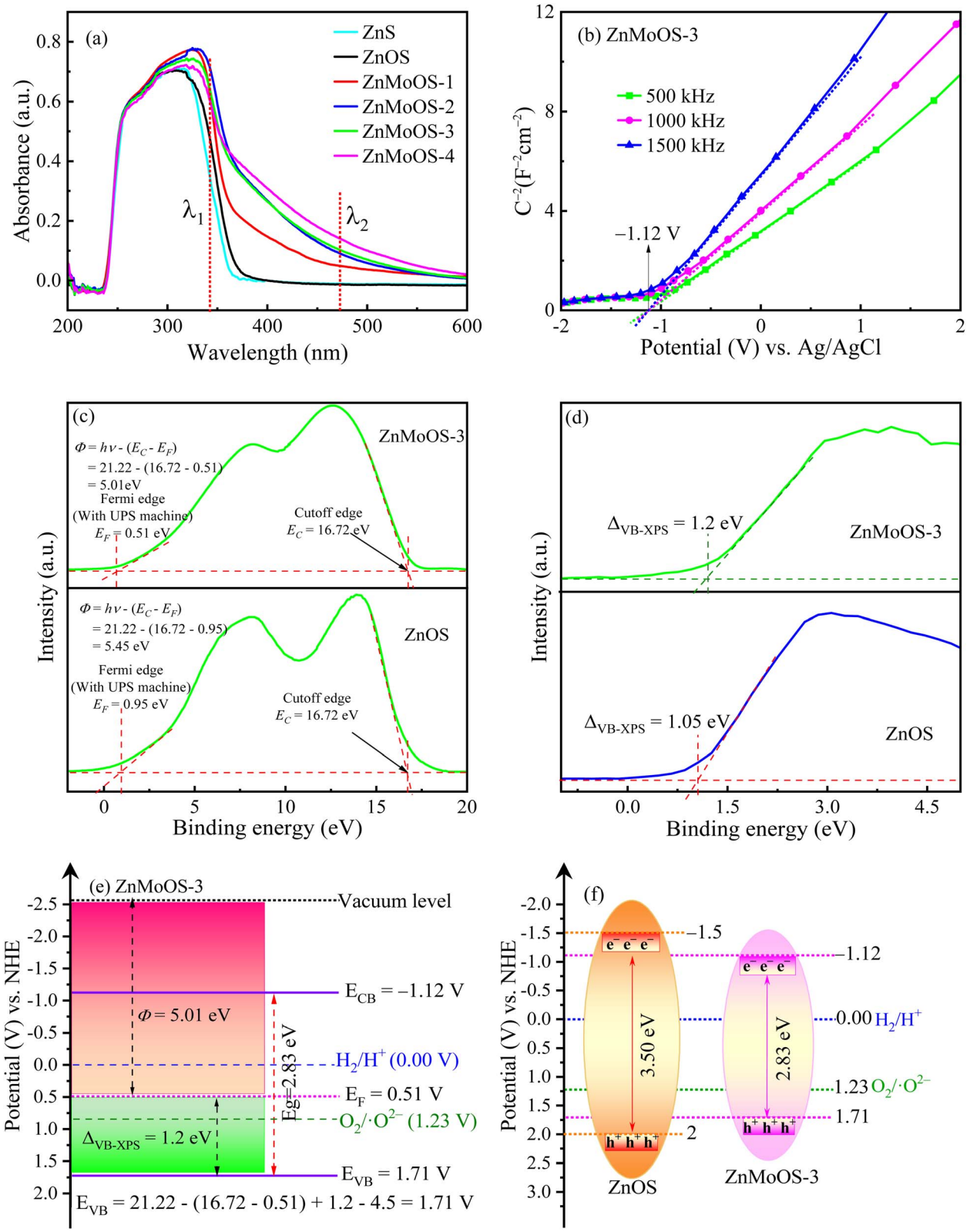

Fig. 3 (a) UV-vis absorption spectra, (b) MS curves of ZnMoOS-3, (c) UPS spectra of ZnMoOS-3 and ZnOS, (d) VB-XPS spectra of ZnMoOS-3 and ZnOS, and (e) energy band arrangement of ZnMoOS-3. (f) Schematic band structures of ZnOS and ZnMoOS-3.

can be attributed to the lattice distortion of ZnOS induced by the co-doping of Mo and O. Meanwhile, hydrazine regulation gives rise to heterovalent states. As the ratio of $n(Mo^{4+})/n(Mo^{4+} + Mo^{6+})$ increases, more Mo^{4+} ions replace Mo^{6+}, creating a charge imbalance that leads to the formation of Vs. These defects act as electron-capture centers, enhancing the electron transfer and

generating new energy levels within the forbidden band. Consequently, the bandgap decreases, and the wavelength range of light absorption expands. This enables ZnMoOS materials to absorb a broader spectrum of photons, thereby significantly enhancing the utilization efficiency of solar energy.

Fig. 3b displays positive slopes of MS curves. A significant finding confirms that ZnMoOS-3 belongs to n-type semiconductors. This is a crucial characteristic of its application as a photocatalyst. The flat-band potential (U_{fb}) of ZnMoOS-3 is measured at −1.12 V *vs.* Ag/AgCl. Fig. S3† provides U_{fb} values of ZnMoOS-1, ZnMoOS-2, ZnMoOS-4, ZnOS and ZnS, which are −0.99, −1.04, −1.08, −1.50, and −1.33 V, respectively. Utilizing relevant formulae, $U_{CB} = U_{fb} - 0.2$ V *vs.* Ag/AgCl and $V_{NHE} = V_{Ag/AgCl} + 0.2$, $U_{VB} = U_{CB} + E_g$, the U_{CB} of ZnMoOS-3 is calculated to be −1.12 V, and its U_{VB} is determined to be 1.71 V. UPS measured the work function (Φ) of ZnMoOS-3 and ZnOS (Fig. 3c and d). The secondary electron cut-off edge (E_C) and Fermi-level edge (E_F) are 17.22 eV and 0.51 eV for ZnMoOS-3 and 16.72 eV and 0.95 eV for ZnOS-1. As the formula $\Phi = h\nu - (E_C - E_F)$ states, the Φ values of ZnMoOS-3 and ZnOS are 4.51 and 5.45 eV. VB-XPS spectra of ZnMoOS-3 further verified the value of the valence band top (V_{BM}), with a difference of 1 eV between the Fermi level and V_{BM}, estimating the V_{BM} level of ZnMoOS-3 to be 6.21 eV. With the definitions of vacuum at −4.5 eV and NHE at 0.0 eV, the E_{VB} value of ZnMoOS-3 at vacuum was 1.71 eV *vs.* NHE and the E_{CB} value was −1.12 eV, consistent with NHE results. ZnMoOS-3 has a CB position more negative than H^+/H_2 relative to the H^+/H_2 potential at 0.0 eV, enabling water decomposition to H_2.

For a comparative purpose, the energy band diagrams of ZnOS and ZnMoOS-3 are shown in Fig. 3f. For ZnOS, the E_g of is 3.50 eV, $E_{CB} = -1.5$ V, and $E_{VB} = 2.0$ V, and for ZnMoOS-3, the E_g is 2.83 eV, $E_{CB} = -1.12$ V, and $E_{VB} = 1.71$ V. The Mo/O doping resulted in a bandgap value reduction from 3.50 to 3.0 eV, and adding an optimum amount of hydrazine decreased the bandgap value from 3.50 eV to 2.83 eV. Herein, we demonstrate the suitability of ZnMoOS-3 for the photo-HER in visible light. ZnMoOS-3 was obtained *via* Mo/O co-doping and hydrazine modulation of the energy-band structure of ZnS, thereby significantly enhancing the activity of the photo-HER and convincing us of its potential in visible light photocatalysis.

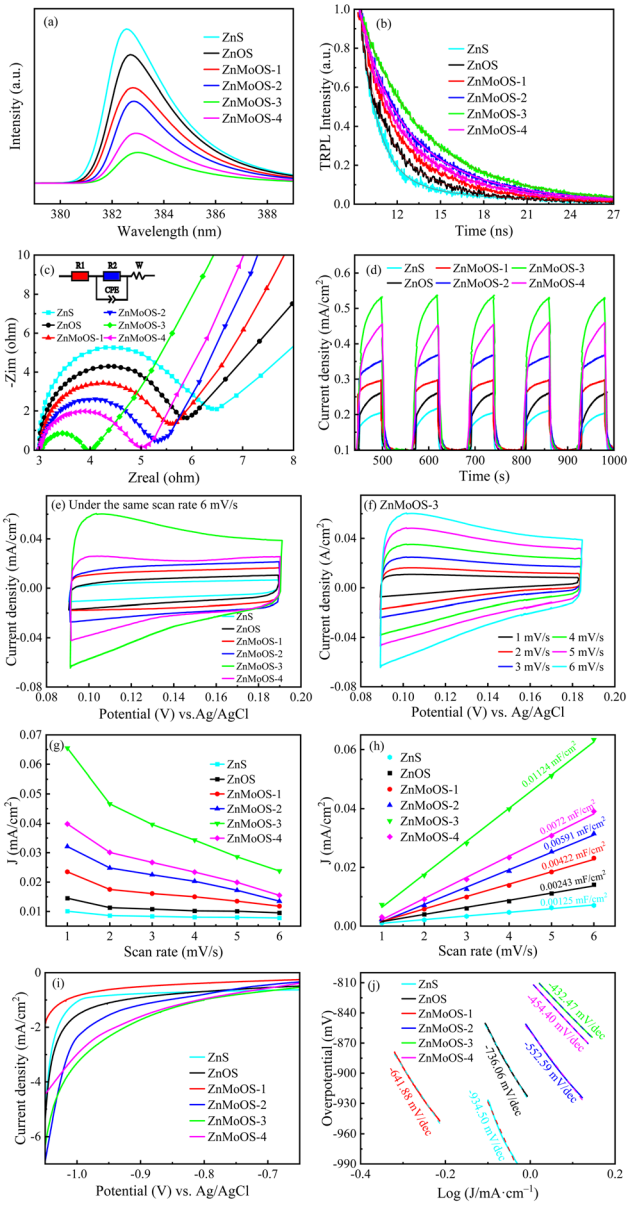

Fig. 4 (a) PL, (b) TRPL, (c) EIS, (d) TPC, and (e) CV curves of ZnMoOS, ZnOS, and ZnS at a scan rate of 6 mV s^{-1} (f) CV curves of ZnMoOS-3 at scan rates of 1, 2, 3, 4, 5, and 6 mV s^{-1}. (g) Specific capacitance, (h) ECSA, (i) LSV, and (j) Tafel curves of ZnMoOS, ZnOS, and ZnS.

3.4 Electrochemical analysis

The data in Fig. 4a demonstrate that the photoluminescence (PL) spectra of all samples are similar in shape. It can also be observed that ZnS exhibits a strong emission peak, indicating severe recombination of photo-induced carriers in ZnS.[65] In contrast, ZnMoOS-3 has the lowest PL intensity, suggesting that the incorporation of Mo suppresses the photo-induced electron–hole recombination and improves the charge separation efficiency. As shown in Fig. 4b, time-resolved photoluminescence (TRPL) spectroscopy was employed to evaluate the carrier lifetimes of ZnMoOS, ZnOS, and ZnS. The average lifetime was retrieved by curve fitting with the formula:[56] $\tau_{ave} = (A_1\tau_1^2 + A_2\tau_2^2)/(A_1\tau_1 + A_2\tau_2)$, and A_1, τ_1, A_2, and τ_2 are given in Table S4.† The average carrier lifetime of ZnMoOS-3 is 4.250 ns, while those of ZnOS and ZnS are 1.314 and 1.216 ns, respectively. This indicates that Mo doping enhances the carrier separation efficiency, suppresses charge recombination, and thus prolongs the lifetime of photo-induced carriers to improve the photo-HER performance. Meanwhile, the effective separation of photo-induced electrons/holes pairs and interfacial charge transfer ability in catalysts were investigated through electrochemical measurements. Fig. 4c presents the EIS curves of ZnS, ZnOS, and ZnMoOS. The diameter of the semicircle in the Nyquist diagram determines the photo-induced carrier transfer resistivity. Among them, ZnMoOS-3 exhibits the smallest diameter, indicating that the resistivity is decreased and the charge transfer rate is accelerated after Mo doping.[66,67]

To further certify the enhanced carrier transfer rate of ZnMoOS-3, TPC density analysis was employed to investigate photo-induced electrons/holes pair separation. Higher photocurrent can promote the separation and intensity of photoresponse, thereby enhancing the photo-HER performance.[68] Fig. 4d shows the TPC densities of ZnS, ZnOS, and ZnMoOS with different Mo-doped contents. Compared to ZnOS, Mo-doped ZnOS exhibits a better photocurrent response intensity in the extended visible light response range after Mo-doping and formation of charge imbalance *via* hydrazine regulation of Mo heterovalence, which increases active sites and promotes photo-induced electron separation. Fig. 4e shows ZnMoOS-1, -2, -3, -4, ZnOS, and ZnS at a scan rate of 6 mV s^{-1}, with ZnMoOS-3 exhibiting the strongest current density. Fig. 4f depicts the CV curves of ZnMoOS-3 at scan rates of 1–6 mV s^{-1}, showing an increase in the current density with increasing scan rate. The current density values of ZnMoOS-1, ZnMoOS-2, ZnMoOS-4, ZnOS, and ZnS are presented in Fig. S4.† It can be observed that the order of the current density is as follows: ZnMoOS-3 > ZnMoOS-2 > ZnMoOS-4 > ZnMoOS-1 > ZnOS > ZnS. This result strongly indicates that the ZnMoOS-3 electrode possesses a favorable electron transfer rate. Fig. 4g depicts the specific capacitance curves of ZnMoOS, ZnOS, and ZnS. With the increase in the scanning speed, the specific capacitance decreases, resulting in large currents, and polarization at high scanning speeds results in low specific capacitance. At a considerable scanning speed, the ions in the catalyst move too slowly to respond, and the ions will have insufficient time to use the catalyst, leading to surface adsorption and low specific capacitance. However, the specific capacitance of ZnMoOS-3 was found to be larger than that of other catalysts, which was ascribed to possession of heterovalent states and Vs in ZnMoOS-3, increasing the reactive active sites to maintain the reoxidation state as much as possible, and at high scan speeds, ions had more time to utilize the material, making the specific capacitance of ZnMoOS-3 higher than that of other catalysts. As shown in Fig. 4h, the C_{dl} measurements for ZnS, ZnOS, and ZnMoOS-1, -2, -3, -4 are 1.25, 2.43, 4.22, 5.91, 11.24, and 7.2 μF cm^{-2}, respectively. The maximum C_{dl} was observed for ZnMoOS-3 and the minimum for ZnS. Due to the larger specific surface area and more heterovalent states of ZnMoOS-3, a charge imbalance is created, leading to the formation of sulfur vacancies, which increase the active sites. Fig. 4i presents the current density between −1.05 V and −0.4 V per electrode, as recorded by linear voltammetry (LSV). ZnMoOS-3 exhibited the highest cathodic current density for H_2 generation by water decomposition, indicating a fast photo-generated carrier transfer rate at the ZnMoOS-3 interface.[69,70] Furthermore, Fig. 4j displays a plot of Tafel slopes converted by LSV, showing that the Tafel slopes of ZnMoOS-1, ZnMoOS-2, ZnMoOS-3, ZnMoOS-4, ZnOS, and ZnS are −641.88, −552.59, −432.47, −454.40, −736.06, and −934.50 mV dec^{-1}, respectively, of which the overpotential of ZnMoOS-3 is the smallest, suggesting that it possesses better electron transfer performance in redox reactions.

Our findings indicate that ZnMoOS-3, particularly with the best hydrazine content, exhibits the fastest electron transfer rate and the least electrochemical impedance to reduce the photoelectron–hole recombination rate. These characteristics underscore the excellent photo-HER activity and stability of ZnMoOS-3, highlighting its potential in the field of photo-HER.

3.5 Photocatalytic activity and stability

Fig. 5a shows the photo-HER rate in the presence of 50 mg of catalyst as 1.53, 1.75, 2.08, 1.3, 1.09 and 0.89 mmol h^{-1} for ZnMoOS-1, -2, -3, -4, ZnOS, and ZnS, respectively, and no H_2 was detected in the absence of light and a sacrificial agent. Fig. 5b shows the photo-HER activity of ZnMoOS, ZnOS, and ZnS under visible light. It can be observed that after 6 h of reaction, ZnMoOS-3 evolves the highest hydrogen amount of 12.48 mmol. This is attributed to hydrazine regulation, which produces heterovalent Mo^{4+}/Mo^{6+} states, results in charge re-distribution in the system, promotes electron transfer rate and Vs formation, and thus improves the charge carrier separation and transfer efficiency. ZnMoOS-3 shows the best photo-HER activity, consistent with its electrochemical characteristics of the lowest resistance and highest photocurrent response. Fig. 5c shows the photo-HER results of ZnMoOS-3 after six runs, and it is observed that the photo-HER rate decreases from 12.82 mmol to 12.14 mmol without a noticeable significant change, further proving that ZnMoOS-3 has good stability during the photo-HER. Table S5† presents the research on the photo-HER of ZnS-based catalysts in recent years. In comparison with previous studies, it can be observed that ZnMoOS-3 has a superior photo-HER performance. Fig. S5† illustrates the variation of the photo-HER rate with the amount of catalyst for ZnMoOS-1, ZnMoOS-2, ZnMoOS-3, ZnMoOS-4, ZnOS, and ZnS. It can be observed from this figure that a nonlinear relationship exists between the amount of catalyst and the reaction rate. Fig. S6† demonstrates the influence of solution pH on the photo-HER rate. Specifically, under strongly acidic conditions, the photo-HER rate decreases. Under weakly acidic conditions with a pH value of 6.5, the photo-HER rate reaches its maximum value. Under alkaline conditions, the photo-HER rate also shows a downward trend. This can be attributed to the fact that under highly acidic conditions, the reaction between H^+, Na_2S, and Na_2SO_3 leads to a reduction in the H^+ concentration, which subsequently causes a decrease in the hydrogen ion adsorption efficiency.[71] Under strongly alkaline conditions, the relatively low H^+ concentration results in a low hydrogen ion adsorption efficiency. However, under weakly acidic conditions, the increase in the H^+ content can promote adsorption and combination rates of H^+ on the catalyst surface. Fig. S7† presents the relationship between UV-vis absorption and AQE in terms of radiation wavelengths of ZnMoOS-3. It can be observed that the AQE at 400 nm is 18.6%, and the AQE can be detected at 560 nm.

The stability of ZnMoOS-3, confirmed through multiple tests, provides a reliable foundation for its potential applications in photocatalysis and materials science, reassuring the audience of its performance consistency over time. To further validate the stability of ZnMoOS-3, we examined its XRD spectrum before and after six runs (Fig. 5d). The peak intensity and position showed no significant change, confirming the stability

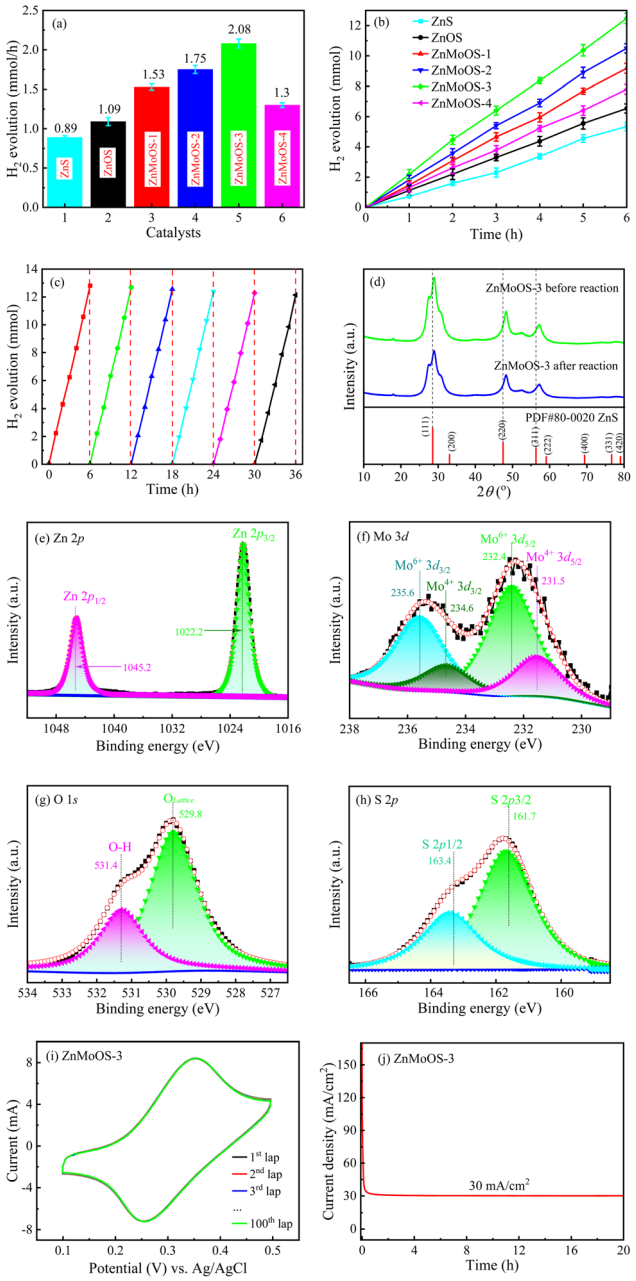

Fig. 5 (a and b) Hydrogen production from ZnMoOS, ZnOS and ZnS. (c) Photo-HER activity of the recycled ZnMoOS-3 catalyst. (d) XRD pattern and (e) Zn 2p, (f) Mo 3d, (g) O 1s, and (h) S 2p XPS spectra of the ZnMoOS-3 catalyst after six cyclic runs. (i) 100 CV cyclic tests at 50 mV s^{-1} in a redox solution and (j) electrochemical long-term stability of ZnMoOS-3.

of ZnMoOS-3. Fig. 5e–h present the Zn 2p, Mo 3d, O 1s, and S 2p XPS spectra of ZnMoOS-3 after six repeated uses, revealing little change in XPS peaks with the progress of the photoreaction. Fig. 5i displays the electrochemical CV curves of ZnMoOS-3 after 100 cycles of a redox reaction, exhibiting stable redox peaks, indicating little change in the potential and current density of the electrochemical reduction/oxidation. Fig. 5j shows the long-term electrochemical stability of ZnMoOS-3 operated at 1.5 V and 30 mA cm^{-2}, further confirming its good stability.

3.6 Density functional theory calculations

To further validate that the Mo doping and heterovalent Mo^{4+}/Mo^{6+} states enhance the photo-HER activity, ZnOS and ZnMoOS-3 models were selected as representative examples for detailed DFT investigations (Fig. 6 and S8†). Conductivity, a critical parameter for evaluating the electrochemical activity of electrocatalysts, was assessed by calculating the band structures of the ZnOS and ZnMoOS-3 models. As shown in Fig. S8c and d,† the computed bandgaps were 3.54 and 2.85 eV, respectively, closely matching the experimental values of 3.5 eV for ZnOS and 2.83 eV for ZnMoOS-3.

To further elucidate the electronic structure of ZnOS and ZnMoOS-3, electron localization functions (ELFs) were computed, and the results are shown in Fig. 6a and b. ELF values close to 0.5 indicate ionic bonding, while values near 0.8 or 0 suggest covalent or metallic bonding. In both the ZnOS and ZnMoOS-3 models, atomic bonding is predominantly ionic, with Mo atoms in the ZnMoOS-3 model also exhibiting ionic characteristics. The results reveal that Mo^{4+}/Mo^{6+} doping in ZnOS significantly enhances the electron distribution in the vacancy region (Fig. 6b). This moderate electron localization within the vacancy region facilitates effective interaction with H atoms, suggesting a strong orbital overlap between the catalyst and the H 1s orbital.[72–74] To better understand why ZnMoOS-3 exhibits the best catalytic performance, we calculated the band structure and ELF for ZnMoOS-1 (Fig. S9†). The results indicate that Mo^{4+}/Mo^{6+} doping in ZnOS significantly enhances the electron distribution in the vacancy regions. However, the degree of electron concentration remains lower than that observed in ZnMoOS-3. Consequently, while photo-HER activity of ZnMoOS-1 is improved compared to pristine ZnOS, it remains inferior to that of ZnMoOS-3.

The adsorption behavior of H^+ on Zn and non-Zn sites was evaluated for the ZnOS model, revealing that H^+ adsorption is more energetically favorable on Zn sites, thereby promoting proton adsorption and hydrogen evolution. Similarly, in the ZnMoOS-3 model, H^+ adsorption was more favourable on the Mo^{4+} site than on other sites. Reaction pathways for the photo-HER were further analysed using free energy diagrams for H* adsorption on ZnOS and ZnMoOS-3 (Fig. 6c). The free energy for H* adsorption on ZnMoOS-3 was calculated to be −0.063 eV, closer to 0 compared to −0.106 eV for ZnOS. According to the Sabatier principle,[75–81] these results suggest that ZnMoOS-3 achieves a more balanced hydrogen binding energy, which facilitates the desorption of H_2 and thereby enhances the overall photo-HER kinetics. These findings are consistent with experimental photo-HER measurements, where ZnOS exhibits lower hydrogen evolution efficiency than ZnMoOS-3.

Charge analysis was conducted to investigate further the stable adsorption of H* on ZnOS and ZnMoOS-3. The charge density difference (CDD) maps (Fig. 6d and e) and Bader charge analysis provide an intuitive representation of electron transfer and catalytic activity. Following Mo doping in ZnOS, enhanced electron transfer from ZnMoOS-3 to H* was observed. This enhancement is attributed to the reduced bandgap and increased electron distribution, which improve light absorption

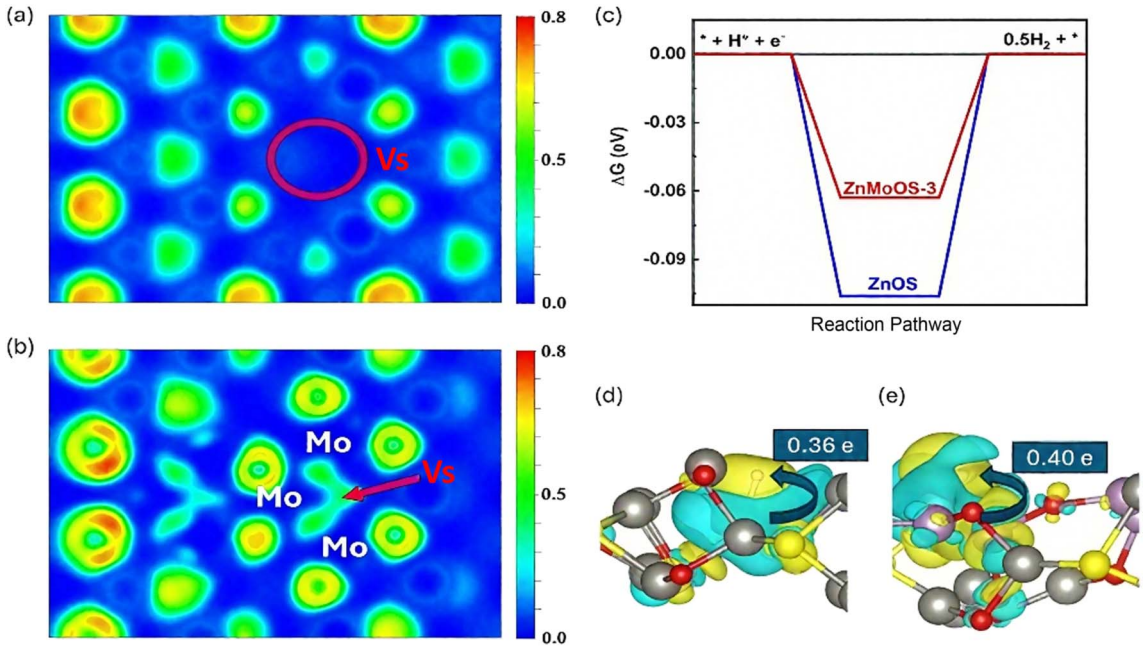

Fig. 6 The ELF plots for (a) ZnOS and (b) ZnMoOS-3. 0 and 0.8 represent the electron deficiency and electron abundance, respectively. (c) Calculated ΔG values of the HER on ZnOS and ZnMoOS-3. The CDD maps of (d) ZnOS and (e) ZnMoOS-3. The isovalue is 0.0008 eÅ^{-3}.

and enhance the photo-HER activity. These results prove that the Mo doping and heterovalent Mo^{4+}/Mo^{6+} states significantly enhance the photo-HER activity in ZnMoOS.

3.7 Photo-HER kinetic mechanism

Fig. 7a illustrates the photo-HER mechanism of ZnMoOS, with Vs defects playing a crucial role. These defects provide reactive active centers that activate H_2O molecules, reducing their activation energy for the photo-HER. Additionally, Vs defects capture electrons and adsorb polar H_2O molecules under coulombic interaction to promote photo-generated charge separation and form active oxygen at Vs sites through the photo-HER, which weakens the O–H bonding of adsorbed H_2O molecules, producing H_2. Furthermore, the charge variation with the formation of Mo^{4+} accelerates the charge transfer and promotes the photo-HER.[82,83] The kinetic mechanism of ZnMoOS photo-HER include the following steps: (I) Vs defects trap H_2O;[84,85] (II) the Mo^{6+}/Mo^{4+} valence transition occurs *via* an electron jump between Mo^{4+} and Mo^{6+}, thus extending the e^- lifetime and promoting electron transfer for the photo-HER;[86,87] (III) H_2O donates electrons, breaking H–O to give active oxygen while releasing H_2. (IV) Vs is recovered by the $h^+/O_{active}/S^{2-}/SO_3^{2-}$ reaction.[88,89]

$$\text{ZnMoOS-3} \xrightarrow{h\nu} h^+ + e^- \quad (1)$$

$$H_2O + Vs^{2+} \rightarrow 2H^+ + O_{active} \quad (2)$$

$$2H^+ + 2e^- \rightarrow H_2\uparrow \quad (3)$$

$$H_2O + Vs^{2+} + 2e^- \rightarrow H_2\uparrow + O_{active} \quad (4)$$

$$2S^{2-} + 2h^+ \rightarrow S_2^{2-} \quad (5)$$

$$S_2^{2-} + SO_3^{2-} \rightarrow S_2O_3^{2-} + S^{2-} \quad (6)$$

$$S_2O_3^{2-} + 3O_{active} + 4h^+ \rightarrow 2SO_3^{2-} + 3\ Vs^{2+} \quad (7)$$

The adsorption sites of water were further explored through Raman spectroscopy. As depicted in Fig. 7b, the Raman spectral peaks within the 200–400 cm^{-1} range correspond to the A_1/E_1 transverse optical and A_1/E_1 longitudinal optical phonons of the Zn–S bonds in the catalyst.[90] Notably, for ZnMoOS-3, two new peaks emerge at 575 cm^{-1} and 930 cm^{-1}. The peak at 575 cm^{-1} can be attributed to the A_1 longitudinal optical phonons of Zn–O bonds,[91] while the 930 cm^{-1} peak corresponds to the symmetric stretching vibration of Mo–O bonds. Compared with the symmetric stretching vibration peak of standard Mo–O bonds (940 cm^{-1}), this peak exhibits a shift towards lower frequencies,[92] which is likely attributable to the presence of sulfur vacancies in ZnMoOS-3. Fig. 7c presents an enlarged view of the Raman spectra in the 200–400 cm^{-1} region for ZnMoOS-3 and ZnS. It is evident that the peak intensity of ZnMoOS-3 decreases, and there is a noticeable shift towards lower frequencies. This observation provides further evidence for sulfur vacancies in ZnMoOS-3.[93–95] Furthermore, as illustrated in Fig. 7d, distinct peaks are observed when water molecules adsorb on ZnMoOS-3 and ZnS. For ZnMoOS-3, the asymmetric stretching vibration of O–H at 3700 cm^{-1} shifts to lower frequencies with increased intensity. Additionally, the symmetric stretching vibration peak of O–H not only shifts to lower frequencies but also splits. These changes indicate that the adsorption environment of water molecules on ZnMoOS-3

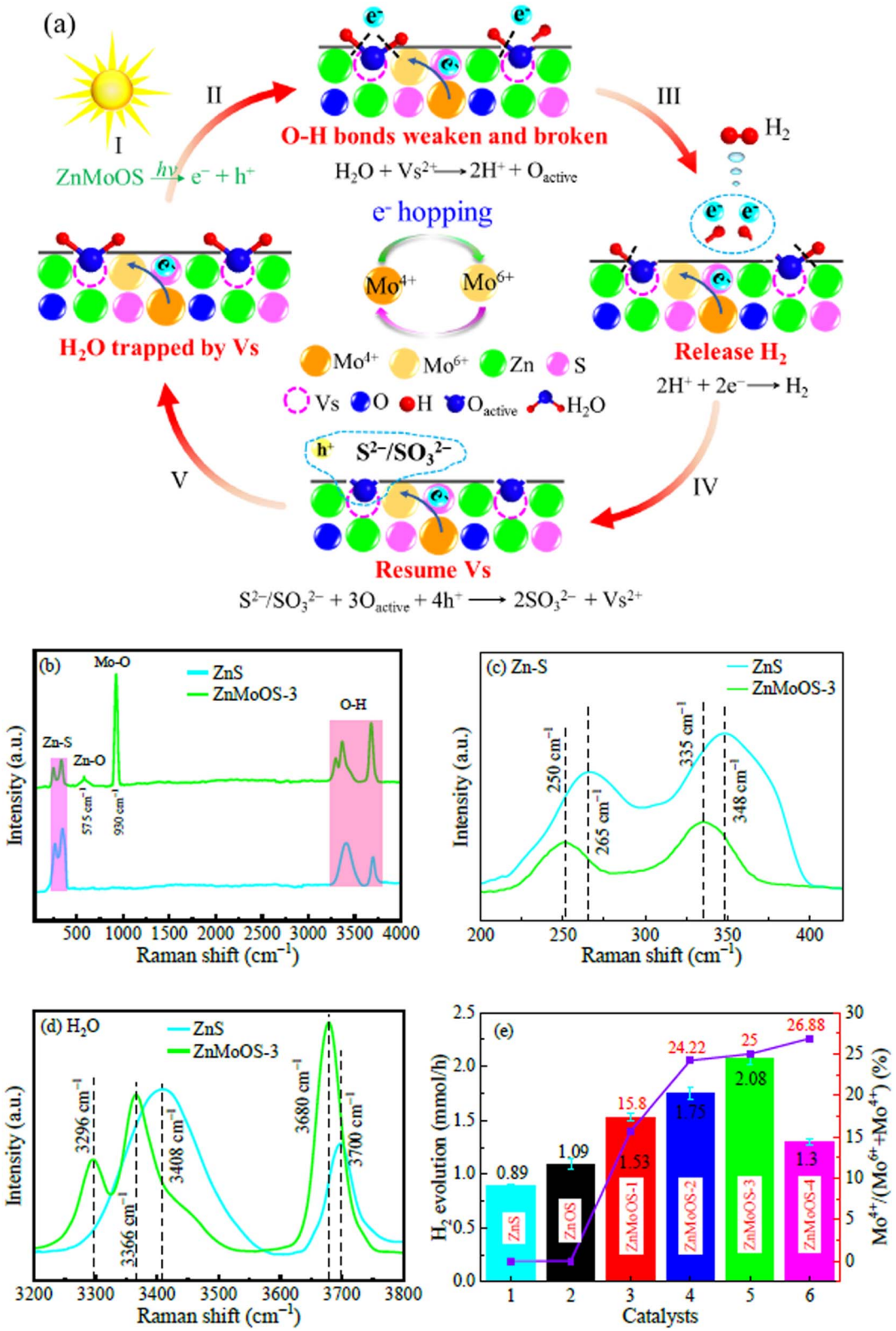

Fig. 7 (a) Schematic illustration of the reaction kinetic mechanism of the photo-HER over ZnMoOS-3 with Vs. (b) Raman spectra of ZnS and ZnMoOS-3. Local enlarged Raman spectra of (c) Zn–S bond and (d) O–H bond. (e) Correlation between the photo-HER and $n(Mo^{4+})/n(Mo^{4+} + Mo^{6+})$ ratio in ZnS, ZnOS, and ZnMoOS.

has been altered,[96] which can be attributed to the adsorption effect of sulfur vacancies present in ZnMoOS-3 on water molecules.

Fig. 7e shows the relationship between the photo-HER and change ratio in $n(Mo^{4+})/n(Mo^{4+} + Mo^{6+})$ for various valence states. Fig. 7b indicates that with hydrazine introduction, the $n(Mo^{4+})/n(Mo^{4+} + Mo^{6+})$ ratio increases, and photo-HER activities of ZnMoOS-1, ZnMoOS-2, and ZnMoOS-3 catalysts also increase. However, when $n(Mo^{4+})/n(Mo^{4+} + Mo^{6+})$ reaches 26.88%, the photo-HER activity of ZnMoOS-4 is lower than that of ZnMoOS-3. According to the results of the PL and TRPL tests, it can be observed that the PL peak intensity of ZnMoOS-4 is higher than that of ZnMoOS-3, and the average carrier lifetime of ZnMoOS-4 is lower than that of ZnMoOS-3. This indicates that the separation efficiency of photo-generated carriers in ZnMoOS-4 is lower than that in ZnMoOS-3. Meanwhile, by analyzing the results of electrochemical tests, ZnMoOS-3 exhibits a better electron transfer efficiency. Therefore, when ZnMoOS-4 has a higher content of heterovalent states, it shows a lower photo-HER.

4. Conclusions

A novel Mo/O co-doped ZnS oxysulfide catalyst with abundant Vs defects and heterovalent Mo^{4+}/Mo^{6+} states was synthesized *via* a facile method. ZnMoOS-3 with appropriate Mo/O co-doping and driven by the optimum hydrazine content exhibits an excellent photo-HER rate of 41.6 mmol g^{-1} h^{-1} and an AQE of 18.6% at 400 nm, along with good stability and durability. The Mo/O co-doping reduces the E_g of ZnS and extends its visible-light absorption range. The hydrazine-driven process adjusts ZnMoOS with appropriate bivalent $n(Mo^{4+})/n(Mo^{6+})$ states and creates abundant Vs defects. The Vs defects are active sites to capture H_2O molecules and weaken H–O–H bonds for producing protons and H_2 generation. The bivalent $n(Mo^{4+})/n(Mo^{6+})$ states act as hosts for photogenerated electrons, facilitating the rapid hopping of photogenerated electrons between $Mo^{4+} \leftrightarrow Mo^{6+}$ to transfer for the photo-HER, thereby improving the photo-HER efficiency. DFT calculations indicate that Mo/O co-doping of ZnMoOS with abundant Vs defects and heterovalent Mo^{4+}/Mo^{6+} states significantly facilitates hydrogen desorption and enhances the surface *H generation rate. This work provides a strategy for leveraging vacancy defects and heterovalent states to design stable and photocorrosion-resistant sulfide catalysts for an efficient photo-HER.

Data availability

The authors declare that all relevant data are included in the manuscript and ESI.†

Conflicts of interest

The authors declare that they have no known competing financial interests or personal relationships that could have appeared to influence the work reported in this paper.

Acknowledgements

This work was supported by the National Natural Science Foundation of China under grant no. 31000269, the Natural Science Foundation of Fujian Province under grant no. 2021J01100, and the Forestry Department Foundation of Fujian Province under grant no. (2023TG17 and 2025FKJ18).

References

1 Z. Su, C. Ye, Y. Xu, B. Wu, D.-H. Kuo, X. Wu, B. Yang, P. Zhang, L. Chen, D. Lu, J. Lin, Z. Yuan and X. Chen, Synergistic vacancy defects and the surface hydrophobic-to-superhydrophilic wetting engineering in W/S co-doped BiOI for enhanced photocatalytic hydrogen evolution, *Chem. Eng. J.*, 2024, **496**, 154282.
2 P. Kuang, T. Tong, K. Fan and J. Yu, In Situ Fabrication of Ni-Mo bimetal sulfide hybrid as an efficient electrocatalyst for hydrogen evolution over a wide pH range, *ACS Catal.*, 2017, **7**, 6179–6187.
3 A. B. Abdeta, F. Wedajo, Q. Wu, D.-H. Kuo, P. Li, H. Zhang, T. Huang, J. Lin and X. Chen, B and N co-doped cellulose-supported Ag-/Bi-doped $Mo(S,O)_3$ trimetallic sulfo-oxide catalyst for photocatalytic H_2 evolution reaction and 4-nitrophenol reduction, *Langmuir*, 2024, **40**, 12987–13000.
4 J. Wang, C. Zhou, J. Wu and T. Zhang, Facile fabrication of TT-T Nb_2O_5 heterophase junctions via in situ phase transformation towards enhanced photocatalytic H_2-production activity, *J. Mater. Chem. A*, 2024, **12**, 4123–4128.
5 J. Wang, J. Wang, R. Shi, C. Zhou and T. Zhang, Facile Fabrication of N-doped $K_2Nb_2O_6$ nanocrystals with defective pyrochlore structure for improved visible-light photocatalytic hydrogen production, *Small Struct.*, 2023, **4**, 2200105.
6 D. Ma, M. Yin, M. Xue and Y. Fan, Detailed studies on characterization and photocatalytic hydrogen production of ammonium tetrathiomolybdate and tetrathiotungstate pyrolysis products, *J. Solid State Chem.*, 2024, 124609.
7 B. Wu, B. Yang, X. Wu, D.-H. Kuo, Z. Su, L. Chen, P. Zhang, M. T. Mosisa, D. Lu, Z. Yuan, J. Lin and X. Chen, Synergistic tuning of heterovalent states and oxygen vacancy defect engineering in hydrophilic W-doped Sb_2OS_2 for enhanced nitrogen photoreduction to ammonia, *ACS Appl. Mater. Interfaces*, 2024, **16**, 58764–58779.
8 P. K. Panda, B. Sahoo and S. Ramakrishna, Electrospun nanofibers for photocatalytic water treatment and hydrogen generation application: A review, *Int. J. Hydrogen Energy*, 2023, **48**, 37193–37208.
9 L. Chen, P. Zhang, D.-H. Kuo, J. Jiang, B. Wu, Z. Su, O. A. Zelekew, J. Lin, D. Lu and X. Chen, Synergism of heterovalent valence state and oxygen vacancy defect engineering in Co/S co-doped TiO_2 for nitrogen photoreduction to ammonia, *J. Mater. Chem. A*, 2024, **12**, 9871–9885.
10 A. Fujishima and K. Honda, Electrochemical photolysis of water at a semiconductor electrode, *Nature*, 1972, **238**, 37–38.

11 S. K. Lakhera, R. T. Pangal, H. Y. Hafeez and B. Neppolian, Oxygen-functionalized and Ni^{x+} (x=2,3)-coordinated graphitic carbon nitride nanosheets with long-life deep-trap states and their direct solar-light-driven hydrogen evolution activity, *Chemsuschem*, 2019, **12**, 4293–4303.

12 D. A. Abraham, A. Rajan, M. D. Dhileepan, M. Anpo and B. Neppolian, Nitrogen doped graphene supported mixed metal sulfide photocatalyst for high production of hydrogen using natural solar light, *Catal. Today*, 2023, **423**, 113971.

13 L. Shang, B. Tong, H. Yu, G. I. N. Waterhouse, C. Zhou, Y. Zhao, M. Tahir, L. Wu, C. Tung and T. Zhang, CdS nanoparticle-decorated Cd nanosheets for efficient visible light-driven photocatalytic hydrogen evolution, *Adv. Energy Mater.*, 2016, **6**, 1501241.

14 T. Tsuyoshi and D. Kazunari, Particulate photocatalysts for water splitting: Recent advances and future prospects, *ACS Energy Lett.*, 2019, **4**, 542–549.

15 A. R. M. Shaheer, V. Vinesh, S. K. Lakhera and B. Neppolian, Reduced graphene oxide as a solid-state mediator in TiO_2/$In_{0.5}WO_3$ S-scheme photocatalyst for hydrogen production, *Sol. Energy*, 2021, **213**, 260–270.

16 M. Dong, P. Zhou, C. Jiang, B. Cheng and J. Yu, First-principles investigation of Cu-doped ZnS with enhanced photocatalytic hydrogen production activity, *Chem. Phys. Lett.*, 2017, **668**, 1–6.

17 H. Abdullah, R. T. Ginting, H. Shuwanto and D.-H. Kuo, Banana peel biowaste-derived carbon composited with Zn(O,S) for solar-light photocatalytic hydrogen generation, *Int. J. Hydrogen Energy*, 2022, **47**, 41021–41033.

18 H. Abdullah, H. Shuwanto and D.-H. Kuo, Multifunctional Ni-Mg bimetal-activated Zn(O,S) for hydrogen generation and environmental remediation with simulated solar-light irradiation, *Catal. Sci. Technol.*, 2021, **11**, 7200–7216.

19 B. Wu, X. Wu, D.-H. Kuo, X. Tang, X. Mao, B. Yang, Z. Su, P. Zhang, L. Chen, M. Liu, J. Lin and X. Chen, W/Br co-doped ZnOS with Zn/O bi-vacancy defects and heterovalent states for enhanced photocatalytic hydrogen evolution, *Mater. Today Energy*, 2025, **49**, 101828.

20 H. Abdullah, N. S. Gultom, H. Shuwanto, W. L. Kebede and D.-H. Kuo, Self-protonated Ho-doped Zn(O,S) as a green chemical conversion catalyst to hydrogenate nitro to amino compounds, *ACS Appl. Mater. Interfaces*, 2020, **12**, 43761–43770.

21 H. Abdullah, N. S. Gultom and D.-H. Kuo, Synthesis and characterization of La-doped Zn(O,S) photocatalyst for green chemical detoxification of 4-nitrophenol, *J. Hazard. Mater.*, 2019, **363**, 109–118.

22 H. Shuwanto, H. Abdullah, D.-H. Kuo and N. S. Gultom, Surface active sites of Y-doped Zn(O,S) for chemisorption and hydrogenation of azobenzene and nitroaromatic compounds under light via self-generated proton, *Appl. Surf. Sci.*, 2021, **552**, 149508.

23 H. Abdullah and D.-H. Kuo, Utilization of photocatalytic hydrogen evolved (Zn,Sn)(O,S) nanoparticles to reduce 4-nitrophenol to 4-aminophenol, *Int. J. Hydrogen Energy*, 2019, **44**, 191–201.

24 B. Poornaprakash, P. Puneetha, S. Sangaraju, Y. J. Yeon, B. A. Al-Asbahid, D. Y. Lee, S. Ramu and Y. L. Kim, Hydrogen evolution properties: Cr doping and V co-doping effect of ZnS nanoparticles, *Mater. Lett.*, 2023, **340**, 134186.

25 B. Poornaprakash, H. Park, K. Subramanyam, S. V. P. Vattikuti, K. C. Devarayapalli, S. H. Nam, Y. L. Kim, M. S. Pratap-Reddy, M. G. Hahm and V. R. Minnam-Reddy, Doping-induced photocatalytic activity and hydrogen evolution of ZnS: V nanoparticles, *Ceram. Int.*, 2021, **47**, 26438–26446.

26 B. Poornaprakash, P. R. Puneetha, M. S. Pratap, S. Sambasivam, P. Rosaiah, B. A. Al-Asbahi, D.-Y. Lee and Y. L. Kim, Hydrogen evolution properties of Cr doped and (Cr, Er) co-doped ZnS nanoparticles, *J. Mater. Sci.: Mater. Electron.*, 2023, **34**, 1614.

27 E. M. Jubeer, M. A. Manthrammel, P. A. Subha, M. Shkir, K. P. Biju and S. A. AlFaify, Defect engineering for enhanced optical and photocatalytic properties of ZnS nanoparticles synthesized by hydrothermal method, *Sci. Rep.*, 2023, **13**, 2045–2322.

28 P. Miao, J. Zhao, R. Shi, Z. Li, Y. Zhao, C. Zhou and T. Zhang, Layered double hydroxide engineering for the photocatalytic conversion of inactive carbon and nitrogen molecules, *ACS EST Engg.*, 2022, **2**, 1088–1102.

29 Y. Zhao, G. Chen, T. Bian, C. Zhou, G. I. N. Waterhouse, L. Wu, C. Tung, L. J. Smith, D. O'Hare and T. Zhang, Photoreduction: defect-rich ultrathin ZnAl-layered double hydroxide nanosheets for efficient photoreduction of CO_2 to CO with water, *Adv. Mater.*, 2015, **27**, 7823.

30 Y. Zhao, C. Chang, F. Teng, Y. Zhao, G. Chen, R. Shi, G. I. N. Waterhouse, W. Huang and T. Zhang, Defect-engineered ultrathin δ-MnO_2 nanosheet arrays as bifunctional electrodes for efficient overall water splitting, *Adv. Energy Mater.*, 2017, **7**, 1700005.

31 V. Gurylev and T. P. Perng, Defect engineering of ZnO: Review on oxygen and zinc vacancies, *J. Eur. Ceram. Soc.*, 2021, **41**, 4977–4996.

32 T.-C. Huang, X. Chen, G. S. Wolde and D.-H. Kuo, Photocatalytic hydrogen production over highly oxygen deficient Cu-doped TiO_2 and its composites: Insights of kinetic reaction micromechanisms, *Sep. Purif. Technol.*, 2024, **339**, 126671.

33 P. Zhang, L. Chen, D.-H. Kuo, B. Wu, Z. Su, D. Lu, Q. Wu, J. Li, J. Lin and X. Chen, Photocatalytic fixation of nitrogen to ammonia with Ce/S co-doped TiO_2 catalyst: Synergistic tuning of heterovalent metal states and oxygen vacancy defects, *J. Mater. Chem. A*, 2024, **12**, 7163–7177.

34 J. Wang, Z. Wang, B. Huang, Y. Ma, Y. Liu, X. Qin, X. Zhang and Y. Dai, Oxygen vacancy induced band-gap narrowing and enhanced visible light photocatalytic activity of ZnO, *ACS Appl. Mater. Interfaces*, 2012, **4**, 4024–4030.

35 U. Shah, F. A. Jan, R. Ullah, A. Wajidullah, N. Ullah and M. Ahmad, Photocatalytic degradation of acidic and basic dye by ZnS and tin-doped ZnS nanocatalysts, *Iran. J. Sci.*, 2023, **47**, 2731–8109.

36 G.-J. Lee, H. Chen and J. J. Wu, (In, Cu) Co-doped ZnS nanoparticles for photoelectrochemical hydrogen production, *Int. J. Hydrogen Energy*, 2019, **44**, 110–117.
37 L. Bao, Y. Dong, C. Dai, G. Xu, Y. Yang, X. liu, D. Ma, Y. Jia and C. Zeng, Optimizing the electronic structure of ZnS via cobalt surface doping for promoted photocatalytic hydrogen production, *Inorg. Chem.*, 2021, **60**, 15712–15723.
38 S. Liu and X. Chen, Preparation and characterization of a novel activated carbon-supported N-doped visible light response photocatalyst, *J. Chem. Technol. Biotechnol.*, 2007, **82**, 453–459.
39 J. Zhang, J. Yu, M. Jaroniec and J. Gong, Noble metal-free reduced graphene oxide-$Zn_xCd_{1-x}S$ nanocomposite with enhanced solar photocatalytic H_2-production performance, *Nano Lett.*, 2012, **12**, 4584–4589.
40 P. Li, Q. Wu, Q. Ji, A. B. Abdeta, D.-H. Kuo, T. Huang, H. Zhang, O. A. Zelekew, J. Lin and X. Chen, Sulfur-doped $Sb_4Mo_{10}O_{31}$ bimetallic sulfur-oxide catalyst for highly efficient reduction of toxic organic and hexavalent chromium under dark, *J. Environ. Chem. Eng.*, 2023, **11**, 110700.
41 A. Khlyustova, N. Sirotkin, A. Kraev, T. Kusova, V. Titov and A. Agafonov, Mo-doped TiO using plasma in contact with liquids: advantages and limitations, *J. Chem. Technol. Biotechnol.*, 2021, **96**, 1125–1131.
42 X. Chen, M. Qi, Y. Li, Z. Tang and Y. Xu, Enhanced ambient ammonia photosynthesis by Mo-doped Bi_5O_7Br nanosheets with light-switchable oxygen vacancies, *Chin. J. Catal.*, 2021, **42**, 2020–2026.
43 Q. Xue and H. Fan, Mo-modified $BiOI_{0.5}Cl_{0.5}$ composites preparation for antibiotic removal, *Mater. Today Commun.*, 2024, **39**, 108873.
44 H. Wang, G. Wang, Y. Chen, X. Shen, Y. Lv and Q. Nie, Advantages of $Mo_{4.9}(Sb_2Te)_{95.1}$ film with improved crystallization properties for phase change memory, *Mater. Lett.*, 2015, **161**, 240–243.
45 L. Zuo, R. Li, Q. Liu, Y. Duan, H. Wang, H. Fan, B. Li and L. Wang, In situ Mo-doped $ZnIn_2S_4$/Ni–Ni Hofmann-type coordination polymer composites for photocatalytic hydrogen evolution reaction, *J. Colloid Interface Sci.*, 2024, **661**, 207–218.
46 M. S. Tamboli, S. S. Patil, D.-K. Lee, C. S. Praveen, A. M. Tamboli, U. Sim, K. Lee, G. H. Gu and C. Park, Dynamic role of dopant and graphene on $BiVO_4$ photoanode for enhanced photoelectrochemical hydrogen production, *Energy*, 2024, **298**, 131329.
47 Y. Li, S. Zhu, Y. Liang, Z. Li, S. Wu, C. Chang, S. Luo and Z. Cui, One-step synthesis of Mo and S co-doped porous g-C_3N_4 nanosheets for efficient visible-light photocatalytic hydrogen evolution, *Appl. Surf. Sci.*, 2021, **536**, 147743.
48 N. Su, Y. Bai, Z. Shi, J. Li, Y. Xu, D. Li, B. Li, L. Ye and Y. He, ReS_2 Cocatalyst Improves the Hydrogen Production Performance of the CdS/ZnS Photocatalyst, *ACS Omega*, 2023, **8**, 6059–6066.
49 F. Qiao, W. Liu, J. Yang, J. Yuan, K. Sun and P. Liu, Hydrogen production performance and theoretical mechanism analysis of chain-like ZnO/ZnS heterojunction, *Int. J. Hydrogen Energy*, 2023, **28**, 953–963.
50 C. Du, Q. Zhang, Z. Lin, B. Yan, C. Xia and G. Yang, Half-unit-cell $ZnIn_2S_4$ monolayer with sulfur vacancies for photocatalytic hydrogen evolution, *Appl. Catal., B*, 2019, **248**, 193–201.
51 Y. Tan, Z. Chai, B. Wang, S. Tian, X. Deng, Z. Bai, L. Chen, S. Shen, J. Guo, M. Cai, C. Au and S. Yin, Boosted photocatalytic oxidation of toluene into benzaldehyde on $CdIn_2S_4$-CdS: synergetic effect of compact heterojunction and S-vacancy, *ACS Catal.*, 2021, **11**, 2492–2503.
52 H. Yang, A. Meng, L. Yang and Z. Li, Construction of S-scheme heterojunction consisting of $Zn_{0.5}Cd_{0.5}S$ with sulfur vacancies and $Ni_xCo_{1-x}(OH)_2$ for highly efficient photocatalytic H_2 evolution, *Chem. Eng. J.*, 2022, **432**, 134371.
53 Y. Ma, G. Hai, D. G. Atinafu, W. Dong, R. Li, C. Hou and G. Wang, Carbon inserted defect-rich MoS_{2-x} nanosheets@CdS nanospheres for efficient photocatalytic hydrogen evolution under visible light irradiation, *J. Colloid Interface Sci.*, 2020, **569**, 89–100.
54 X. Wang, X. Wang, J. Huang, S. Li, A. Meng and Z. Li, Interfacial chemical bond and internal electric field modulated Z-scheme Sv-$ZnIn_2S_4$/$MoSe_2$ photocatalyst for efficient hydrogen evolution, *Nat. Commun.*, 2021, **12**, 4112.
55 X. Wu, P. Zhang, B. K. Insua, B. Yang, D.-H. Kuo, D. Lu, M. T. Mosisa, J. Lin and X. Chen, V-/O-doping to endow Ag_2S-based bimetal oxysulfide with sulfur vacancies and heterovalent states for rapid reduction of organic and Cr(VI) pollutants in the dark, *Adv. Sustain. Syst.*, 2025, **9**, 2400771.
56 A. B. Abdeta, H. Sun, Y. Guo, Q. Wu, J. Zhang, Z. Yuan, J. Lin and X. Chen, A novel AgMoOS bimetallic oxysulfide catalyst for highly efficiency catalytic reduction of organic dyes and chromium (VI), *Adv. Powder Technol.*, 2021, **32**, 2856–2872.
57 L. Bao, Y. Jia, X. Ren, X. Liu, C. Dai, S. Ali, M. Bououdina, Z. Lu and C. Zeng, Cr dopants and S vacancies in ZnS to trigger efficient photocatalytic H_2 evolution and CO_2 reduction, *J. Mater. Sci. Technol.*, 2024, **199**, 75–85.
58 P. Zhang, Q. Wu, H. Wang, Y. Xu, Y. Lai, P. Li, D.-H. Kuo, T. Huang, H. Zhang, M. T. Mosisa, J. Li, J. Lin, X. Chen and D. Lu, Hydrazine-driven cation valence regulation and oxygen defect engineering in sulfur-doped $CoMoO_4 \cdot 0.9H_2O$ for highly efficient reduction of toxic organics and hexavalent chromium under dark, *Mater. Today Chem.*, 2024, **37**, 102028.
59 S. Liu, C. Chen, Y. Zhang, Q. Zheng, S. Zhang, X. Mu, C. Chen, J. Ma and S. Mu, Vacancy-coordinated hydrogen evolution reaction on MoO_{3-x} anchored atomically dispersed MoRu pairs, *J. Mater. Chem. A*, 2019, **7**, 14466–14472.
60 L. Chen, B. Wu, X. Wu, D.-H. Kuo, T. L. Wan, B. Yang, P. Zhang, Z. Su, J. Lin, D. Lu and X. Chen, Synergistic engineering of heterovalent states and sulfur-vacancy defects in Co/O co-doped ZnS for enhanced photocatalytic hydrogen evolution, *Int. J. Hydrogen Energy*, 2025, **98**, 944–956.

61 L. Yi, F. Nkinahamira, H. Jiang, J. Huang, Y. Ma and R. Zhu, Mo_2N decorated hierarchical $ZnIn_2S_4$ with sulfur-rich vacancy photocatalyst for efficient photocatalytic hydrogen production, *J. Environ. Chem. Eng.*, 2023, **11**, 110240.

62 X. Chen, H. Sun, J. Zhang, O. A. Zelekew, D. Lu, D.-H. Kuo and J. Lin, Synthesis of visible light responsive iodine-doped mesoporous TiO_2 by using biological renewable lignin as template for degradation of toxic organic pollutants, *Appl. Catal., B*, 2019, **252**, 152–163.

63 M. Ibrahim, M. Zayed, A. M. Ahmed, M. A. Ghanem, M. Shaban, S. A. Elkhalik and F. Mohamed, Synthesis and characterization of Mo-doped PbS thin films for enhancing the photocatalytic hydrogen production, *Mater. Chem. Phys.*, 2024, **315**, 128962.

64 H. Sun, A. B. Abdeta, D.-H. Kuo, Q. Wu, Y. Guo, O. A. Zelekew, Z. Yuan, J. Lin and X. Chen, Activated carbon supported Cu*Sn*OS catalyst with an efficient catalytic reduction of pollutants under dark condition, *J. Mol. Liq.*, 2021, **334**, 116079.

65 X. Chen, D.-H. Kuo and D. Lu, N-doped mesoporous TiO_2 nanoparticles synthesized by using biological renewable nanocrystalline cellulose as template for the degradation of pollutants under visible and sun light, *Chem. Eng. J.*, 2016, **295**, 192–200.

66 P. Zhang, H. Wang, Y. Lai, Y. Xu, L. Chen, Q. Wu, D.-H. Kuo, D. Lu, M. T. Mosisa, J. Li, J. Lin and X. Chen, Synergistic Co/S co-doped CeO_2 sulfur-oxide catalyst for efficient catalytic reduction of toxic organics and heavy metal pollutants under dark conditions, *J. Water Process Eng.*, 2024, **58**, 104820.

67 X. Chen, P. Zhang, D. H. Kuo, Q. Wu, A. B. Abdeta, B. Wu, Z. Su, L. Chen, O. A. Zelekew and J. Lin, Material design in converting an oxidative-type $BiVO_4$ catalyst into a reductive $BiV(S,O)_{4-x}$ sulfo-oxide catalyst for nitrogen photoreduction to ammonia, *J. Mater. Chem. A*, 2023, **11**, 19091–19106.

68 Y. Yang, S. Zhao, F. Bi, J. Chen, Y. Wang, L. Cui, J. Xu and X. Zhang, Highly efficient photothermal catalysis of toluene over Co_3O_4/TiO_2 p–n heterojunction: The crucial roles of interface defects and band structure, *Appl. Catal., B*, 2022, **315**, 121550.

69 Z. Su, B. Wu, C. Li, D.-H. Kuo, P. Zhang, L. Chen, D. Lu, J. Lin, X. Chen and Z. Yuan, Mn/S co-doped BiOCl regulated with a hydrophobic-to-superhydrophilic transition and oxygen-vacancy defects for assisting photocatalytic hydrogen evolution, *Chem. Eng. J.*, 2025, **510**, 161621.

70 A. B. Abdeta, F. Wedajo, Q. Wu, D.-H. Kuo, P. Li, H. Zhang, T. Huang, J. Lin and X. Chen, Activated carbon anchoring site enrichment through B and N co-doping for boosting $Bi_2Mo_{2.5}(S,O)_{10}$ oxysulfide catalyst stability and visible-light-driven hydrogen evolution, *Adv. Sustain. Syst.*, 2024, **8**, 2400128.

71 Z. Su, X. Wu, D.-H. Kuo, B. Yang, B. Wu, L. Chen, P. Zhang, J. Lin, D. Lu and X. Chen, Synergistic vacancy defects and bandgap engineering in an Ag/S co-doped Bi_2O_3-based sulfur oxide catalyst for efficient hydrogen evolution, *J. Mater. Chem. A*, 2024, **12**, 10494–10506.

72 X. Liu, Z. Jiang and Y. Guo, Mechanistic understanding on effect of doping nitrogen with graphene supported single-atom Ir toward HER and OER: A computational consideration, *Chem. Phys. Lett.*, 2024, **834**, 140971.

73 B. Li, C. Xiao, N. M. Harrison, R. M. Fogarty and A. P. Horsfield, Role of electron localisation in H adsorption and hydride formation in the Mg basal plane under aqueous corrosion: a first-principles study, *Phys. Chem. Chem. Phys.*, 2023, **25**, 5989–6001.

74 H. Huang, C. Xue, Z. Fang, Z. Wang, B. Luo, M. Sun, L. Zhou, K. Hu, J. Kou and L. Wang, Bridging localized electron states of pyrite-type CoS_2 cocatalyst for activated solar H_2 evolution, *Nano Res.*, 2022, **15**, 202–208.

75 Y. Liu, Z. Sun and Y. H. Hu, Bimetallic cocatalysts for photocatalytic hydrogen production from water, *Chem. Eng. J.*, 2021, **409**, 128250.

76 Z. Ye, Z. Xu, W. Yue, X. Liu, L. Wang and J. Zhang, Exploiting the LSPR effect for an enhanced photocatalytic hydrogen evolution reaction, *Phys. Chem. Chem. Phys.*, 2023, **25**, 2706–2716.

77 S. Khan, X. Dai, T. Ali, S. Mahmood, M. ul Haq, M. S. Riaz and Y. Hu, Recent advances on photo-thermo-catalysis for carbon dioxide methanation, *Int. J. Hydrogen Energy*, 2023, **48**, 24756–24787.

78 T. L. Wan, J. Liu, X. Tan, M. Liu, S. Smith and L. Kou, Bimetallic conjugated metal–organic frameworks as bifunctional electrocatalysts for overall water splitting, *Nanoscale*, 2023, **15**, 10149–10158.

79 T. L. Wan, J. Liu, X. Tan, T. Liao, Y. Gu, A. Du, S. Smith and L. Kou, Rational design of 2D ferroelectric heterogeneous catalysts for controllable hydrogen evolution reaction, *J. Mater. Chem. A*, 2022, **10**, 22228–22235.

80 Y. Cheng, P. Fu, Z. Yu, X. Yang, Y. Zhang, A. Yuan and L. Chen, Modulation of the multiphase phosphorus/sulfide heterogeneous interface via rare earth for solar-enhanced water splitting at industrial-level current densities, *Carbon Neutrality*, 2024, **3**, 873–887.

81 B. Zhai, J. He, H. Li, X. Li, S. Nurmanov, O. Ruzimuradov and L. Li, Integral morphology and structure design of poly (heptazine imide) for efficient utilization of visible light generated charge carriers in proton reduction reactions, *Carbon Neutrality*, 2024, **3**, 888–903.

82 Z. Su, B. Wu, D.-H. Kuo, L. Chen, P. Zhang, B. Yang, X. Wu, D. Lu, J. Lin and X. Chen, Synergistic hydrazine-driven regulation and Mo/S co-doping to endow BiOBr with heterovalent molybdenum states and abundant oxygen vacancy defects for photocatalytic hydrogen evolution, *J. Mater. Chem. A*, 2024, **12**, 28486–28502.

83 Q. Wu, L. Chen, D.-H. Kuo, P. Li, A. B. Abdeta, O. A. Zelekew, J. Lin and X. Chen, Sulfur substitution and defect engineering in an unfavored $MnMoO_4$ catalyst for efficient hydrogen evolution under visible light, *ACS Appl. Mater. Interfaces*, 2023, **15**, 22142–22156.

84 X. Chen, T. Huang, D.-H. Kuo, H. Sun, P. Li, O. A. Zelekew, A. B. Abdeta, Q. Wu, J. Zhang, Z. Yuan and J. Lin, Material design with the concept of solid solution-type defect engineering in realizing the conversion of an

electrocatalyst of NiS_2 into a photocatalyst for hydrogen evolution, *Appl. Catal., B*, 2021, **298**, 120542.

85 X. Chen, H. Sun, D.-H. Kuo, A. B. Abdeta, O. A. Zelekew, Y. Guo, J. Zhang, Z. Yuan and J. Lin, Spherical nanoflower-like bimetallic $(Mo,Ni)(S,O)_{3-x}$ sulfo-oxide catalysts for efficient hydrogen evolution under visible light, *Appl. Catal., B*, 2021, **287**, 119992.

86 X. Chen, Q. Wu, D.-H. Kuo, A. B. Abdeta, H. Zhang, P. Li, T. Huang, O. A. Zelekew and J. Lin, Initiating highly efficient $(Bi,Ce)_2(O,S)_{3-x}$ oxysulfide catalysts with rich oxygen vacancies for hydrogen evolution via adjusting valence band configuration, *J. Mater. Chem. A*, 2023, **11**, 4126–4141.

87 A. B. Abdeta, Q. Wu, D.-H. Kuo, P. Li, H. Zhang, T. Huang, J. Zhang, J. Lin and X. Chen, Mo-/O-deficient $Bi_2Mo_3(S,O)_{12}$ oxysulfide for enhanced visible-light photocatalytic H_2 evolution and pollutant reduction via in-situ generated protons: A case of material design in converting an oxidative $Bi_2Mo_3O_{12}$ catalyst for the reduction, *J. Catal.*, 2022, **413**, 1056–1069.

88 Q. Wu, A. B. Abdeta, D.-H. Kuo, H. Zhang, Q. Lu, J. Zhang, O. A. Zelekew, M. T. Mosisa, J. Lin and X. Chen, A molybdenum sulfo-oxide/cobalt oxysulfide Z-scheme heterojunction catalyst for efficient photocatalytic hydrogen production and pollutant reduction, *J. Mater. Chem. A*, 2022, **10**, 5328–5349.

89 B. Yang, X. Wu, B. K. Inusa, D.-H. Kuo, P. Zhang, C. Li, H. Yu, T. Liu, D. Lu, Z. Yuan, J. Lin and X. Chen, Synergistic effects of heterovalent states, oxygen vacancy defects, and surface wettability engineering in S-doped $AgBi(MoO_4)_2$ for photocatalytic hydrogen evolution, *Chem. Eng. J.*, 2025, **514**, 163151.

90 J. H. Kim, H. Rho, J. Kim, Y.-J. Choi and J.-G. Park, Raman spectroscopy of ZnS nanostructures, *J. Raman Spectrosc.*, 2012, **43**, 906–910.

91 C. Du, Z. Gu, M. Lu, J. Wang, S. Zhang, J. Zhao, G. Cheng, H. Heng and Y. Chen, Raman spectroscopy of (Mn, Co)-codoped ZnO films, *J. Appl. Phys.*, 2006, **99**, 123515.

92 J. Wang, Z. Qing, X. Zhou, H. Zou, H. Li, A. Liu, S. Duan and Y. Li, Crystal structure, Raman spectra, bond characteristics, and microwave dielectric properties of $MnMoO_4$ ceramics, *Ceram. Int.*, 2023, **49**, 23627–23633.

93 F. Wang, H. Li, Q. Wu, J. Fang, Y. Huang, C. Yin, Y. Xu and Z. Luo, Improving the performance of a non-aqueous lithium-air battery by defective titanium dioxides with oxygen vacancies, *Electrochim. Acta*, 2016, **202**, 1–7.

94 J. Li, X. Xu, X. Liu, C. Yu, D. Yan, Z. Sun and L. Pan, Sn doped TiO_2 nanotube with oxygen vacancy for highly efficient visible light photocatalysis, *J. Alloys Compd.*, 2016, **679**, 454–462.

95 W. Yang, C. Li, H. Wang, X. Li, W. Zhang and H. Li, Cobalt doped ceria for abundant storage of surface active oxygen and efficient elemental mercury oxidation in coal combustion flue gas, *Appl. Catal., B*, 2018, **239**, 233–244.

96 M. Dekermenjian, A. Merlen, A. Ruediger and M. Rérat, Water adsorption on MgO surfaces: a vibrational analysis, *Crystals*, 2023, **13**, 1153.